

Measuring topological invariants in polaritonic graphene

P. St-Jean,¹ A. Dauphin,² P. Massignan,^{2,3} B. Real,⁴ O. Jamadi,⁴ M. Milićević,¹ A. Lemaître,¹ A. Harouri,¹ L. Le Gratiet,¹ I. Sagnes,¹ S. Ravets,¹ J. Bloch,¹ and A. Amo⁴

¹*Centre de Nanosciences et de Nanotechnologies (C2N),*

CNRS - Université Paris-Sud / Paris-Saclay, Palaiseau, France

²*ICFO-Institut de Ciències Fotoniques, The Barcelona Institute of Science and Technology, Barcelona, Spain*

³*Departament de Física, Universitat Politècnica de Catalunya, Barcelona, Spain*

⁴*Physique des Lasers, Atomes et Molécules (PhLAM), CNRS - Université de Lille, Lille, France*

Topological materials rely on engineering global properties of their bulk energy bands called topological invariants. These invariants, usually defined over the entire Brillouin zone, are related to the existence of protected edge states. However, for an important class of Hamiltonians corresponding to 2D lattices with time-reversal and chiral symmetry (e.g. graphene), the existence of edge states is linked to invariants that are not defined over the full 2D Brillouin zone, but on reduced 1D sub-spaces. Here, we demonstrate a novel scheme based on a combined real- and momentum-space measurement to directly access these 1D topological invariants in lattices of semiconductor microcavities confining exciton-polaritons. We extract these invariants in arrays emulating the physics of regular and critically compressed graphene, i.e. where Dirac cones have merged. Our scheme provides a direct evidence of the bulk-edge correspondence in these systems, and opens the door to the exploration of more complex topological effects, e.g. involving disorder and interactions.

Topological bands are characterized by integer-valued quantities, called topological invariants, that are typically defined as the integral of a local property (e.g. the Berry curvature) over the full Brillouin zone (BZ). The hallmark of these invariants is their robustness against local perturbations, which endows topological matter with properties that are insensitive to certain types of disorder and defects^{1,2}. One notable example is provided by the edge conductivity plateaus in the quantum Hall effect that can be linked to a topological invariant called the Chern number³.

A distinct situation arises in 2D crystals presenting time-reversal and chiral (or sub-lattice) symmetry, such as honeycomb, Lieb and Kagome lattices. The bands of these materials are either ungapped or present a globally vanishing Berry curvature; they thus can't be described by a non-zero topological invariant defined over the entire BZ such as the Chern number. Yet, for well-defined crystalline terminations, these materials present edge states that can be linked to topological invariants defined over reduced (1D) sub-spaces of the BZ^{4,5}.

So far, these 1D invariants have solely been determined indirectly by probing the emergence of edge states in honeycomb lattices^{6,7}. Yet, they are bulk properties, and one should be able to extract them without relying on measurements localized at an interface. This is critical in several situations where edges are difficult or even impossible to probe, e.g. in disordered lattices^{8,9}.

Extracting topological invariants from the bulk is a very challenging task in solid-state crystals. Hence, artificial materials, e.g. arrays of cold atoms^{10,11} or photonic crystals^{12,13}, are particularly appealing as they allow accessing topological properties of band structures through optical means¹⁴⁻¹⁸. However, techniques previously developed for extracting topological invariants were all designed for invariants defined in a parameter space of the same dimension as the underlying lattice. They

thus can't be adapted straightforwardly for extracting 1D invariants in 2D chiral Hamiltonians.

In this work, we propose and experimentally demonstrate a powerful technique for measuring topological invariants in 2D lattices with chiral symmetry. This novel technique, based on the concept of mean chiral displacement^{19,20}, consists in optically probing the spatial distribution of a wave-packet for a specific momentum component. The experimental implementation of this scheme is realized in patterned semiconductor microcavities confining exciton-polaritons²¹. This system is particularly well suited for this purpose, as it allows accessing both momentum and real space profiles of Bloch modes with simple imaging techniques. Using polaritonic lattices emulating regular²² and critically compressed²³ graphene (i.e. where Dirac cones have merged), we measure these 1D topological invariants and thus provide a direct evidence of the bulk-edge correspondence in these chiral systems. Our results pave the way to the exploration of more complex phenomena in 2D chiral lattices, including disorder- or interaction-induced topological phase transitions.

1D topological invariants of graphene

Chiral symmetry describes periodic arrays formed of two sub-lattices with identical on-site energies, and couplings between distinct sub-lattices only²⁴. Honeycomb lattices, i.e. graphene-like materials, are one of the most notable examples of 2D lattices presenting this symmetry. For specific terminations, graphene presents edge states that can be linked to topological invariants defined in 1D sub-spaces of the BZ, corresponding to cuts along specific momentum directions^{4,5}. Before going into the details of the experimental extraction of these invariants, we first recall how they can be defined and how they can be related to the existence of edge states.

In the sub-lattice basis, the tight-binding Hamiltonian

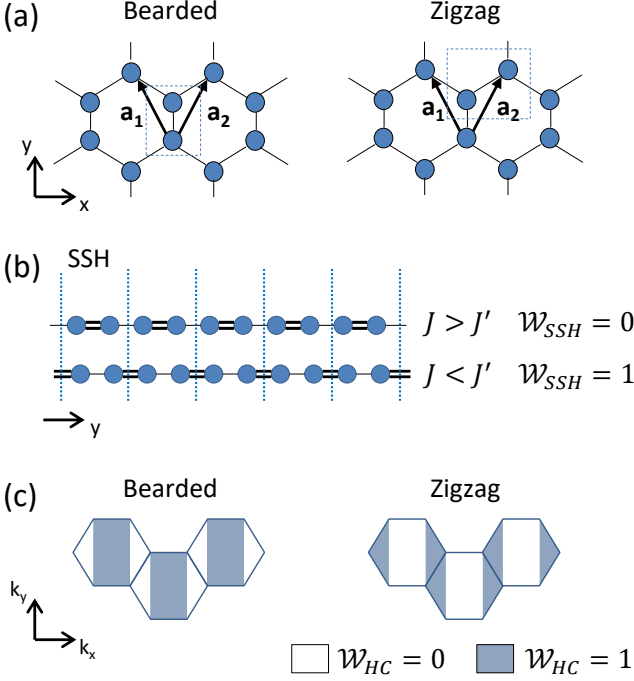


FIG. 1. **Defining winding numbers in graphene.** (a) Definition of the unit cell compatible with bearded and zigzag terminations. $\mathbf{a}_{1,2} = \{\pm 3/\sqrt{2}, 3/2\}$ are the basis vectors of the lattice. (b) Schematic representation of the two topological phases of the SSH model, where $\mathcal{W}_{SSH} = 0$ and $\mathcal{W}_{SSH} = 1$. The dotted lines indicate the boundaries of unit cells. (c) Evolution of the winding number as k_x spans the BZ for bearded and zigzag terminations. Red and blue regions correspond respectively to a winding number of $\mathcal{W}_{HC} = 1$ and $\mathcal{W}_{HC} = 0$.

in momentum space describing a particle hopping on a honeycomb lattice is given by:

$$H_{HC}(\vec{k}) = -t \begin{pmatrix} 0 & g(\vec{k}) \\ g(\vec{k})^\dagger & 0 \end{pmatrix}, \quad (1)$$

where $g(\vec{k}) = 1 + e^{-i\vec{k} \cdot \vec{a}_1} + e^{-i\vec{k} \cdot \vec{a}_2}$, with t the nearest-neighbour hopping amplitude. H_{HC} is defined for a unit cell compatible with bearded edges when considering a finite-sized ribbon along y , with periodic boundary conditions along x , see Fig. 1 (a); for zigzag edges, $g(\vec{k}) = 1 + e^{-i\vec{k} \cdot \vec{a}_2}(1 + e^{i\vec{k} \cdot \vec{a}_1})$. For simplicity, we only consider bearded and zigzag terminations, but the argument and experimental technique developed in this work can be extended to arbitrary edges⁵.

To better understand how 1D topological invariants can be defined for this Hamiltonian, it is insightful to separate explicitly the momentum components parallel (k_x) and perpendicular (k_y) to the edge in $g(\vec{k})$:

$$g(\vec{k}) = J(k_x) + J'(k_x)e^{-i\frac{3}{2}ak_y} \quad (2)$$

where $J(k_x) = 1$ and $J'(k_x) = 2\cos(\frac{\sqrt{3}ak_x}{2})$ for bearded edges, and vice-versa for zigzag edges (including a global phase factor $e^{-i\frac{\sqrt{3}ak_x}{2}}$). For each momentum component k_x , H_{HC} is thus isomorphic, along y , to the Hamiltonian of the well-known Su-Schrieffer-Heeger model (SSH) which represents a 1D dimer chain with different intra-cell (J) and inter-cell (J') coupling energies (see Fig. 1 (b)). For this SSH Hamiltonian, it is possible to define a topological invariant called the winding number \mathcal{W}_{SSH} which is equal to 0 for the dimerization $J > J'$, and equal to 1 for $J < J'$. In the latter case, the non-zero topological invariant is linked to the existence of 0-energy edge states.

In a similar manner, it is possible to define a winding number of H_{HC} for each value of k_x :

$$\mathcal{W}_{HC}(k_x) = \frac{1}{2\pi} \int_{BZ} dk_y \frac{\partial \phi(\vec{k})}{\partial k_y}, \quad (3)$$

where $\phi(\vec{k}) = \arg(g(\vec{k}))$. This 1D topological invariant is equal to the geometric (or Zak) phase picked up by a particle spanning the BZ along k_y , divided by π . It can only take two values: 0 for $|J'/J| < 1$ and 1 for $|J'/J| > 1$, which are equal to the number of edge states for the corresponding momentum component k_x .

Fig. 1 (c) shows calculated values of \mathcal{W}_{HC} as a function of k_x for honeycomb Hamiltonians where the unit cell is compatible with bearded and zigzag terminations. Blue (white) areas correspond to regions where $\mathcal{W}_{HC} = 1$ ($= 0$). For each termination, blue areas indeed correspond to regions of the BZ where the lattice exhibits 0-energy edge states^{5-7,25}. Transitions from one value of the winding number to the other occur at the positions of the Dirac cones: this reflects the fact that the gap needs to close and re-open in order to change a topological invariant.

This mapping between honeycomb and SSH Hamiltonians has only been used so far as a theoretical tool, e.g. for understanding the emergence of edge states^{6,7,26}. Our aim is to directly access these effective SSH Hamiltonians, and measure their winding number as a function of k_x .

Extracting winding numbers of graphene

It was shown in Refs. [19 and 20] that the winding number of any 1D chiral Hamiltonian can be extracted by probing the spatial evolution of an initially localized wave-packet, and computing a quantity called the mean chiral displacement. Hereafter, we demonstrate how this concept can be harnessed for measuring winding numbers in a polaritonic honeycomb lattice. Experimentally, this is realized in an hexagonal lattice of coupled micropillars obtained by etching a semiconductor planar microcavity confining exciton-polaritons (see Fig. 2 (a) and Methods). The coupling of the ground state of each pillar gives rise to two bands emulating the π bands of graphene: a momentum-resolved image of the emission is presented in Fig. 2 (b) showing the presence of Dirac cones.

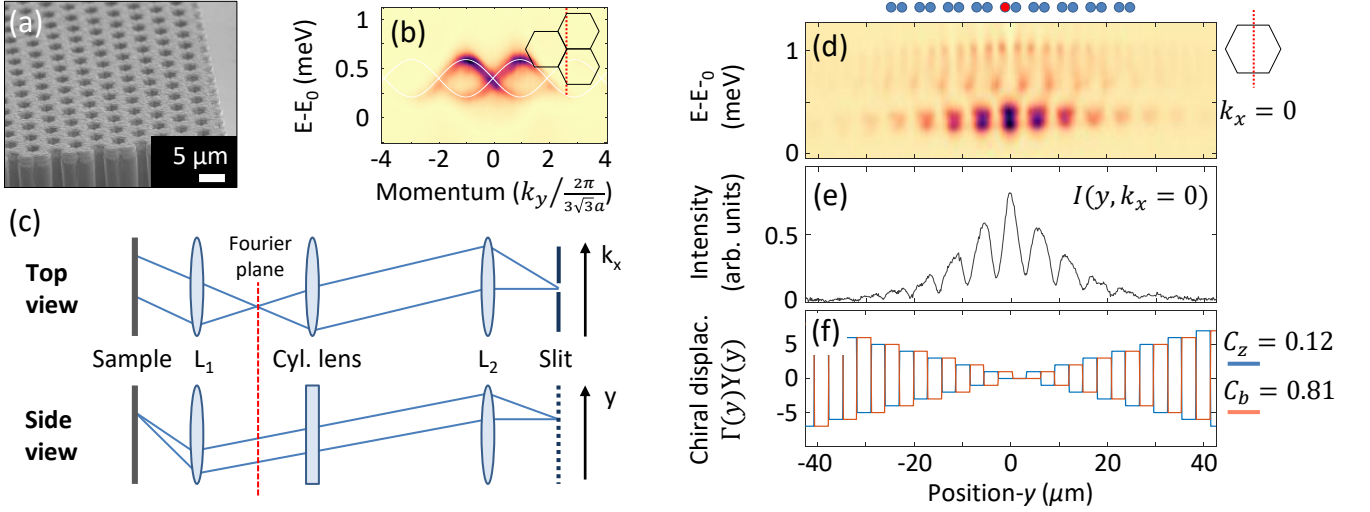


FIG. 2. **Measuring the mean chiral displacement in graphene.** (a) Scanning electron microscopy (SEM) image of a honeycomb lattice of coupled micropillars. (b) Momentum-resolved emission spectra of a polaritonic graphene lattice. The cut in the BZ along which the image is taken is depicted in the inset. (c) Schematic representation of the setup, upper and lower panels depict top and side views. (d) Spatially resolved steady-state emission spectra (along y) for momentum component $k_x \sim 0$. The position of the different sites of the effective SSH lattice is indicated above, where the pumped pillar is in red. (e) Emission intensity integrated over both bands as a function of spatial position. (f) Definition of the chiral displacement ΓY as a function of spatial position. The blue (red) curves correspond to definition of the unit cell compatible with zigzag (bearded) edges. The boundaries of each unit cell are shown by dotted lines of corresponding colours. The values of the mean chiral displacements C_z and C_b extracted from the spectrum presented in Panel (e) are given on the right of this panel.

Our technique for extracting the mean chiral displacement as a function of k_x relies on photoluminescence (PL) measurements with combined real- and momentum-space resolution. The excitation is provided by a non-resonant CW laser focused on a single pillar that generates an incoherent wave-packet spanning both energy bands. We then measure its time-integrated emission profile along y , while filtering a well-defined momentum component along x . This is done using the optical imaging technique described in Fig. 2 (c), where a cylindrical lens (CL) with a curvature along x is positioned at a focal distance of the Fourier plane (red dashed line) of collection lens L_1 . The CL alters light trajectory only along x , providing a Fourier transform of the emission in this direction (upper panel); along y , L_1 and L_2 simply provide real space imaging of the emission (lower panel). Using a vertical slit at the imaging plane, this optical setup thus allows selecting a well-defined value of k_x , while simultaneously accessing the spatial profile along y .

Using this setup, Fig. 2 (d) presents a spatially-resolved (along y) emission profile for a position of the CL selecting momentum component $k_x \sim 0$. This steady-state emission profile clearly describes the physics of a dimer chain with a lower bonding band and an upper anti-bonding band (the position of each effective site is depicted above the panel with the pumped site in red). From this intensity profile, it is then possible to extract the winding number by computing the mean chiral displacement^{19,20} (see Supplementals):

$$\mathcal{C}(k_x) = \int dy \, 2\Gamma(y)Y(y)I^{(\text{int})}(y, k_x) \quad (4)$$

where the integral is taken over the entire emitting region. $I^{(\text{int})}(y, k_x)$ is the energy-integrated spatial profile of the emission (Fig. 2 (e)), $\Gamma(y)$ labels the sub-lattice index of the site (i.e. $+1$ (-1) for the A (B) sub-lattice) and $Y(y)$ labels the index of the unit cell (by definition, the wave-packet is created in the 0^{th} unit cell).

For a finite lattice, the unit cell is defined by the edge. However, for an infinite lattice, the two definitions shown in Fig. 1 (a) are equally valid, and, in the same experiment, we can compute \mathcal{W}_{HC} for unit cells compatible with zigzag and bearded edges just by shifting the definition of Γ . Values of $\Gamma(y)Y(y)$ are presented in Fig. 2 (f) where the blue and red curves are compatible, respectively, with bearded and zigzag terminations. Computation of the mean chiral displacement, for $k_x = 0$, leads to $C_z = 0.12$ for the zigzag unit cell and $C_b = 0.81$ for the bearded one. These values are close to 0 and 1, the theoretical predictions for $k_x = 0$ depicted in Fig. 1 (c). The slight deviation arises from the finite polariton lifetime in 2D lattices, which prevents the wave-packet from reaching a fully balanced distribution over the two sub-lattices, and thus to accurately reflect the chiral symmetry of the underlying array (see Supplementals for a comparison with a 1D lattice where polariton lifetime is typically an order of magnitude longer). Yet, these values are close enough

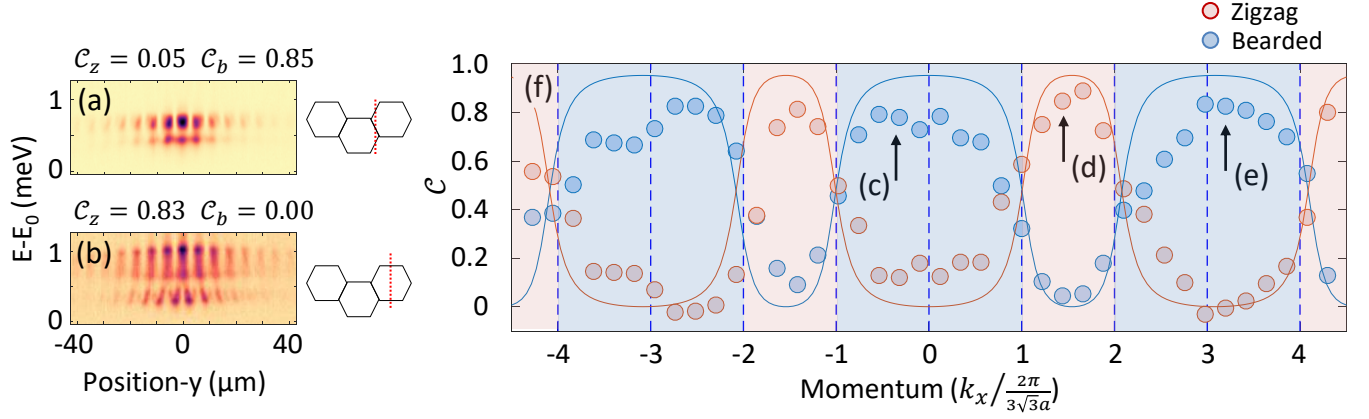


FIG. 3. **Topological phase transitions in graphene.** (a)-(b) Spatially resolved (along y) emission spectra for two distinct momentum components k_x schematically depicted in the inset. Values of C are provided above each panel. (c) Evolution of the mean chiral displacement as a function of k_x . Blue and red circles correspond to values associated to the two possible definitions of the unit cell: respectively bearded and zigzag. Blue (red) shaded areas correspond to regions where $\mathcal{W}_{\text{HC}} = 1$ for a unit cell definition compatible with zigzag (bearded) terminations. Dashed lines indicated the positions of Dirac cones. The solid line represents a theoretical calculation of the mean chiral displacement including losses.

to the ideal ones to enable clearly distinguishing the two topological phases.

Laterally shifting the CL then allows accessing profiles associated to different k_x components. Figure 3 (a) and (b) show spatially resolved emission spectra which are qualitatively very different from the one measured at $k_x = 0$. This reflects the fact that the effective coupling ratio (J'/J) changes with k_x . The emission pattern in Panel (a) exhibits almost flat bands, as one of the two coupling coefficients vanishes thus emulating the physics of a chain of uncoupled dimers. In Panel (b), J'/J is negative, leading to a reversal of the bonding and anti-bonding bands.

Figure 3 (c) present measured values of the mean chiral displacement as a function of k_x , obtained by scanning laterally the CL. Solid lines show numerical calculations of the mean chiral displacement including the effect of polariton lifetime (see Supplementals). These measurements of the mean chiral displacement agree remarkably well with the predicted values of the winding number: each time k_x crosses Dirac cones (indicated by vertical dashed lines), the values of C associated to each definition of the unit cell are exchanged, indicating a topological phase transition. One important consequence of these transitions is the emergence (or disappearance) of 0-energy edge states as a function of k_x . Shaded blue (red) areas correspond to values of k_x where zigzag (bearded) terminations exhibit edge states⁷: these areas are indeed fully compatible with the measured values of \mathcal{W}_{HC} .

Topological characterization of Dirac cones merging in compressed graphene

Having demonstrated the measurement of winding numbers in a honeycomb lattice, we now apply the same technique to a compressed lattice beyond the merging

of Dirac cones. It was shown, both theoretically^{27,28} and experimentally^{29–32}, that applying a uniaxial strain to honeycomb lattices along the y -axis by increasing the hopping amplitude t' with respect to t , as depicted in Fig. 4 (a), shifts the position of the Dirac cones in the band structure along k_x . For strain coefficients $\beta = t'/t > 1$ (i.e. compression), K and K' Dirac cones move toward each other, and merge beyond the critical value of $\beta = 2$, leading to the opening of an energy gap for every k_x . This disappearance of gap closings eliminates the previously observed topological transitions between regions separated by Dirac cones.

To demonstrate this disappearance of phase transitions in critically compressed honeycomb lattices, we fabricate a lattice of coupled micropillars with center-to-center distances $a = 2.4 \mu\text{m}$ and $a' = 1.7 \mu\text{m}$ corresponding to $\beta = 3$ (a SEM image of the lattice is shown in Fig. 4 (b)). Using an identical technique as the one used for regular graphene, Fig. 4 (f) presents the evolution of the values of mean chiral displacement as a function of k_x , for unit cells compatible with zigzag and bearded terminations. Both values of the mean chiral displacement ($C_z \sim 0.1$ and $C_b \sim 0.9$, respectively) are now independent of k_x , indicating the disappearance of topological phase transitions as observed in Fig. 2 (f).

As a result, bearded terminations never present edge states, and zigzag ones do for all values of k_x . This is confirmed by probing the emission near the boundaries of the lattice: Figs. 4 (d) and (e) present PL spectra as a function of momentum along bearded and zigzag terminations, respectively. The cut in momentum space along which these spectra are taken is depicted by the red line in the right inset. For the bearded termination, an edge state delocalized in k_x emerges in the centre of the gap, whereas no state is observed for the zigzag termination. This provides a direct evidence of the

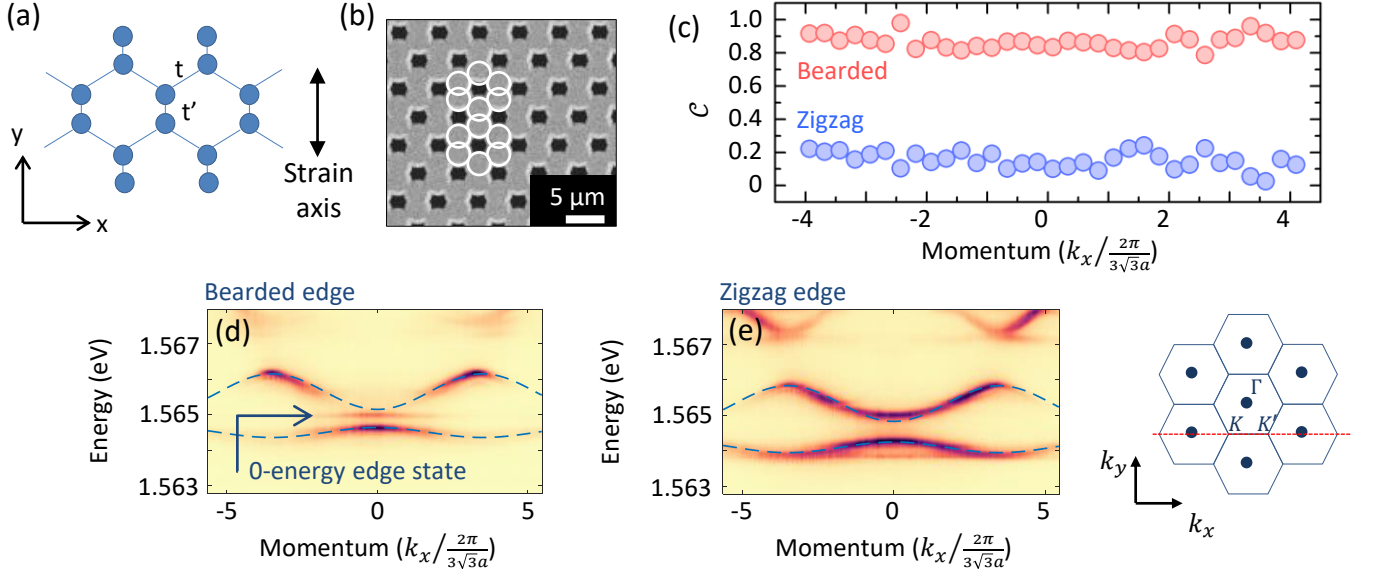


FIG. 4. **Mean chiral displacement in a compressed honeycomb lattice.** (a) Schematic representation of the effect of compression on the lattice. The compression factor is defined as $\beta = J/J'$. (b) Top view SEM image of the compressed honeycomb lattice. White circles are added to indicate the positions of the pillars. (c) Evolution of the mean chiral displacement for both definitions of the unit cell. Blue circles correspond to the definition depicted in Panel (a). (d)-(e) Momentum-resolved PL spectra measured at the boundary of the lattice, along a bearded (d) and a zigzag (e) termination. The cut in the BZ along which these images are taken is depicted in the right inset.

bulk-edge correspondence in this lattice.

Conclusion and outlook

We demonstrated in this work a powerful approach for measuring 1D topological invariants from the bulk of 2D lattices presenting a chiral symmetry. This has allowed probing in honeycomb lattices topological invariants that dictate the existence of edge states. We have also studied critically compressed graphene, where topological phase transitions disappear when Dirac cones merge. One important next step is to extend our scheme to the study of other 2D chiral lattices, e.g. with flat bands^{33,34}, involving orbital^{23,35} or synthetic dimensions³⁶, or presenting higher-order topological phases^{37–40}. Furthermore, the simplicity and versatility of our scheme opens the door to exploring more complex topological effects in polaritonic lattices, e.g. in the presence of disorder or including interactions.

Methods

Sample description. The lattices are etched out of a planar semiconductor cavity with high quality factor ($Q \sim 70000$) consisting of a $\text{Ga}_{0.05}\text{Al}_{0.95}\text{As}$ $\lambda/2$ layer embedded between two $\text{Ga}_{0.05}\text{Al}_{0.95}\text{As}/\text{Ga}_{0.2}\text{Al}_{0.8}\text{As}$ Bragg mirrors formed from 28 (40) pairs in the top (bottom) mirror. Three sets of four GaAs quantum wells of 7 nm width are grown at the three central maxima of the electromagnetic field in the cavity, resulting in strong photon-exciton coupling exhibiting a 15 meV Rabi splitting. After the epitaxy, the cavity is processed by electron beam lithography and dry etching

to form 2-dimensional lattices of overlapping cylindrical micropillars. For the regular honeycomb lattice, the diameter of the pillars is 2.7 μm and centre-to-centre distance is 2.4 μm , allowing for the hopping of polaritons. For the compressed honeycomb lattice, the normal (t) and compressed (t') centre-to-centre distances are respectively 2.4 μm and 2.0 μm .

Experimental technique. Non-resonant PL measurements are realized with a single-mode CW laser at 745 nm. The emission is collected through a microscope objective and imaged on the entrance slit of a spectrometer coupled to a CCD camera with a spectral resolution of $\sim 30 \mu\text{eV}$, using the experimental setup depicted in Fig. 2 (c). The sample is cooled down at $T = 4 \text{ K}$.

Data availability.

The data that support the plots within this paper and other findings of this study are available from the corresponding author upon request.

Acknowledgements.

The authors acknowledge G. Montambaux for fruitful discussions. This work was supported by the H2020-FETFLAG project PhoQus (820392), the QUANTERA project Interpol (ANR-QUAN-0003-05), the French National Research Agency project Quantum Fluids of Light (ANR-16-CE30-0021), the French government through the Programme Investissement d'Avenir (I-SITE ULNE / ANR-16-IDEX-0004 ULNE) managed by the Agence Nationale de la Recherche, the French RENATECH

network, the Labex CEMPI (ANR-11-LABX-0007), the CPER Photonics for Society P4S and the Métropole Européenne de Lille (MEL) via the project TFlight. A.D. and P.M. acknowledge financial support from the Spanish Ministry MINECO (National Plan 15 Grant: FISICATEAMO No. FIS2016-79508-P and FIS2017-84114-C2-1-P, SEVERO OCHOA No. SEV-2015-0522, FPI), European Social Fund, Fundació Cellex, Generalitat de Catalunya (AGAUR Grant No. 2017 SGR1341 and CERCA Program), ERC AdG NOQIA, the National Science Centre, Poland-Symfonia Grant No. 2016/20/W/ST4/00314, the “Juan de la Cierva” fellowship (IJCI-2017-33180), “Ramón y Cajal” program and EU FEDER Quantumcat. P.S.-J. acknowl-

edges financial support from the Marie Skłodowska-Curie individual fellowship ToPol.

Author contributions.

P.S.-J. performed the experiments with help from B.R. and O.J., analysed the data and wrote the manuscript with inputs from all authors. A.D. and P.M. provided critical aspects of the theoretical analysis. M.M. performed preliminary work. A.L., A.H., L.L and I.S grew and processed the sample. S.R. participated in scientific discussions. J.B. and A.A. designed the experiment and supervised the work.

- ¹ Hasan, M. Z. & Kane, C. L. Colloquium: Topological insulators. *Reviews of Modern Physics* **82**, 3045–3067 (2010).
- ² Qi, X. L. & Zhang, S. C. Topological insulators and superconductors. *Reviews of Modern Physics* **83** (2011).
- ³ Thouless, D. J., Kohmoto, M., Nightingale, M. P. & Den Nijs, M. Quantized hall conductance in a two-Dimensional periodic potential. *Physical Review Letters* **49**, 405–408 (1982).
- ⁴ Ryu, S. & Hatsugai, Y. Topological Origin of Zero-Energy Edge States in Particle-Hole Symmetric Systems. *Physical Review Letters* **89**, 077002 (2002).
- ⁵ Delplace, P., Ullmo, D. & Montambaux, G. Zak phase and the existence of edge states in graphene. *Physical Review B - Condensed Matter and Materials Physics* **84** (2011).
- ⁶ Plotnik, Y. *et al.* Observation of unconventional edge states in ‘photonic graphene’. *Nature Materials* **13**, 57–62 (2014).
- ⁷ Miličević, M. *et al.* Edge states in polariton honeycomb lattices. *2D Materials* **2** (2015).
- ⁸ Meier, E. J. *et al.* Observation of the topological Anderson insulator in disordered atomic wires. *Science* **362**, 929–933 (2018).
- ⁹ Stützer, S. *et al.* Photonic topological Anderson insulators. *Nature* **560**, 461–465 (2018).
- ¹⁰ Goldman, N., Budich, J. C. & Zoller, P. Topological quantum matter with ultracold gases in optical lattices. *Nature Physics* **12**, 639–645 (2016).
- ¹¹ Cooper, N. R., Dalibard, J. & Spielman, I. B. Topological bands for ultracold atoms. *Reviews of Modern Physics* **91** (2019).
- ¹² Lu, L., Joannopoulos, J. D. & Soljačić, M. Topological photonics. *Nature Photonics* **8**, 821–829 (2014).
- ¹³ Ozawa, T. *et al.* Topological photonics. *Reviews of Modern Physics* **91** (2019).
- ¹⁴ Atala, M. *et al.* Direct measurement of the Zak phase in topological Bloch bands. *Nature Physics* **9**, 795–800 (2013).
- ¹⁵ Aidelsburger, M. *et al.* Measuring the Chern number of Hofstadter bands with ultracold bosonic atoms. *Nature Physics* **11**, 162–166 (2015).
- ¹⁶ Duca, L. *et al.* An Aharonov-Bohm interferometer for determining Bloch band topology. *Science* **347**, 288–292 (2015).
- ¹⁷ Fläschner, N. *et al.* Experimental reconstruction of the Berry curvature in a Floquet Bloch band. *Science* **352**, 1091–1094 (2016).
- ¹⁸ Wimmer, M., Price, H. M., Carusotto, I. & Peschel, U. Experimental measurement of the Berry curvature from anomalous transport. *Nature Physics* **13**, 545–550 (2017).
- ¹⁹ Cardano, F. *et al.* Detection of Zak phases and topological invariants in a chiral quantum walk of twisted photons. *Nature Communications* **8** (2017).
- ²⁰ Maffei, M., Dauphin, A., Cardano, F., Lewenstein, M. & Massignan, P. Topological characterization of chiral models through their long time dynamics. *New Journal of Physics* **20** (2018).
- ²¹ Carusotto, I. & Ciuti, C. Quantum fluids of light. *Reviews of Modern Physics* **85**, 299–366 (2013).
- ²² Jacqmin, T. *et al.* Direct observation of Dirac cones and a flatband in a honeycomb lattice for polaritons. *Physical Review Letters* **112**, 116402 (2014).
- ²³ Miličević, M. *et al.* Type-III and Tilted Dirac Cones Emerging from Flat Bands in Photonic Orbital Graphene. *Physical Review X* **9** (2019).
- ²⁴ Schnyder, A. P., Ryu, S., Furusaki, A. & Ludwig, A. W. Classification of topological insulators and superconductors in three spatial dimensions. *Physical Review B - Condensed Matter and Materials Physics* **78** (2008).
- ²⁵ Nakada, K., Fujita, M., Dresselhaus, G. & Dresselhaus, M. S. Edge state in graphene ribbons: Nanometer size effect and edge shape dependence. *Physical Review B - Condensed Matter and Materials Physics* **54**, 17954–17961 (1996).
- ²⁶ Ruffieux, P. *et al.* On-surface synthesis of graphene nanoribbons with zigzag edge topology. *Nature* **531**, 489–492 (2016).
- ²⁷ Wunsch, B., Guinea, F. & Sols, F. Dirac-point engineering and topological phase transitions in honeycomb optical lattices. *New Journal of Physics* **10** (2008).
- ²⁸ Montambaux, G., Piéchon, F., Fuchs, J. N. & Goerbig, M. O. Merging of Dirac points in a two-dimensional crystal. *Physical Review B - Condensed Matter and Materials Physics* **80** (2009).
- ²⁹ Tarruell, L., Greif, D., Uehlinger, T., Jotzu, G. & Esslinger, T. Creating, moving and merging Dirac points with a Fermi gas in a tunable honeycomb lattice. *Nature* **483**, 302–305 (2012).
- ³⁰ Rechtsman, M. C. *et al.* Topological creation and destruc-

- tion of edge states in photonic graphene. *Physical Review Letters* **111** (2013).
- ³¹ Bellec, M., Kuhl, U., Montambaux, G. & Mortessagne, F. Topological transition of dirac points in a microwave experiment. *Physical Review Letters* **110**, 033902 (2013).
 - ³² Bellec, M., Kuhl, U., Montambaux, G. & Mortessagne, F. Manipulation of edge states in microwave artificial graphene. *New Journal of Physics* **16**, 113023 (2014).
 - ³³ Jiang, W. *et al.* Topological band evolution between Lieb and kagome lattices. *Physical Review B* **99** (2019).
 - ³⁴ Lim, L.-K., Fuchs, J.-N., Piéchon, F. & Montambaux, G. Dirac points emerging from flat bands in Lieb-kagom'e lattices (2019).
 - ³⁵ Miličević, M. *et al.* Orbital Edge States in a Photonic Honeycomb Lattice. *Physical Review Letters* **118** (2017).
 - ³⁶ Ozawa, T. & Price, H. M. Topological quantum matter in synthetic dimensions. *Nature Reviews Physics* **1**, 349–357 (2019).
 - ³⁷ Peterson, C. W., Benalcazar, W. A., Hughes, T. L. & Bahl, G. A quantized microwave quadrupole insulator with topologically protected corner states. *Nature* **555**, 346–350 (2018).
 - ³⁸ Serra-Garcia, M. *et al.* Observation of a phononic quadrupole topological insulator. *Nature* **555**, 342–345 (2018).
 - ³⁹ Mittal, S. *et al.* Photonic quadrupole topological phases. *Nature Photonics* **13**, 692–696 (2019).
 - ⁴⁰ El Hassan, A. *et al.* Corner states of light in photonic waveguides. *Nature Photonics* **13**, 697–700 (2019).